**Research Article**

# Buoyancy force and magnetic field effects on laminar vortex breakdown and fluid layers

**Brahim MAHFOUD**[1],* , **Mohammed MOUSSAOUI**[1]

[1]*Department of Mechanical, University of MOB-Bouira, Bouira, 10000, Algeria*

**ARTICLE INFO**

**ABSTRACT**

In this study, the Generalized Integral Transformation Technique (GITT) is used to describe the effect of buoyancy force and magnetic field on the vortex breakdown process generated by the rotation of an electrically conductive fluid. A magnetic field is positioned vertically to stabilize the swirling flow caused by the rotation of the bottom disc of a cylindrical recipient. Three fluids were compared in this study where the range of Richardson number is $0 \leq Ri \leq 2.0$. When the temperature difference is greater than $Ri = 0.1$, many layers become visible. These stratified fluid layers act as thermal insulators. In the case of stratification, the increased magnetic field reduces the total number of layers formed in the fluid. The influence of gradient temperature on the distribution of the layers generated is discussed. The limitations between the multilayer structure and the monolayer structure for three fluids are calculated as a function of the flow parameters.

**Cite this article as:** Mahfoud B, Moussaoui M. Buoyancy force and magnetic field effects on laminar vortex breakdown and fluid layers. J Ther Eng 2023;9(1):12–23.

## INTRODUCTION

Flow confined between two disks in which one end disk is rotating and the other is stationary is the simplest state in which vortex breakdown bubbles occur along the symmetry axis. This type of flow is directly applicable to many industrial processes. The results of a visualization experiment first came out by Vogel [1], which exposed that this vortex undergoes breakdown, afterward, Escudier [2] detailed these through an experimental study to take pictures of the internal structure of the flow. There are several studies in the literature examining vortex breakdown and fluid layers [3-5]. Some study is interested in the effect of thermal gradient which is the origin of the increase or decrease of stratification [6-8] and a decrease in the number of Nusselt [9,10].

Recently the magnetic field has been used to suppress vortex breakdown and stabilize the rotating flow. Good crystal quality is achieved in the process of crystal growth under magnetic field control through the melt mass [11]. The magnetic field is also used in the strand-casting process to reduce deficiencies in the finished iron with additional

---

***Corresponding author.**
*E-mail address: mahfoud.mah@gmail.com

*This paper was recommended for publication in revised form by Regional Editor Hasan Köten*

carbon products [12]. Other research, like reference [13], is interested in using the magnetic field to transport the plasma away from the walls of the Tokamak reactor.

The electromagnetic force or Lorentz force is the force to which a charged particle is subjected in an electromagnetic field. This force decreases or increases the axial velocity and therefore affects the rotating flow field. In this case, the Hartmann layer replaces the Ekman layer and the Ekman boundary layer forms in the vicinity of the rotating disc [14]. The challenges of the stability of mixed flow in an enclosed container are discussed in reference [15], which verified that the uniform magnetic field may be employed to control and stabilize fluid motion. Magnetohydrodynamic effects on the counter-rotating flow and co-rotating flow, associated with heat transfer were studied by Mahfoud and Bessaih[16] and Mahfoud et al. [17]. With the help of a magnetic field, Bendjaghlouli et al.[18,19] were able to demonstrate the phenomena of flow stabilization in a liquid metal-filled truncated conical container. As proven by Kharicha et al.[20], the electrical conductivity of the walls is a key element in the flow structure, and it should be given special consideration in some studies, such as in [20].

Some researchers have studied the behavior of vortex breakdown caused by a rotating disk in a cylindrical container in the presence of a magnetic field. [21, 22]. Laouari et al. [23] recently investigated the impact of the axial magnetic field and the conductivities of the walls on the location of breakdown in two regimes (stationary and oscillatory).

Most of the previous studies rely on either finite difference or finite volume schemes to solve governing equations, where a spatial discretization of the domain is required for numerical schemes and an approach for velocity-pressure decoupling. Several researchers try to solve the governing equations using the stream-function, which necessitates the use of a particular scheme to correctly estimate the fourth order of derivatives [24].

In this article, a hybrid technique approach called GITT (Generalized Integral Transform Technique) was employed to solve problems of linear or nonlinear diffusion and convection-diffusion [10, 25, 26, 27]. As discussed in different studies [26,27], this approach may be employed for MHD fluid flow and heat transfer problems.

The first goal is to understand the role of the temperature gradient in vortex breakdown and how it affects the appearance of the layered structure. The second goal is to discover the critical magnitude of Ha for eliminating the layer's structure. As a consequence, domain borders where no layering occurs are established.

## MATHEMATICAL MODELLING MODEL

In this study, a cylindrical container of radius R and height H contains an electrically conductive fluid. Three
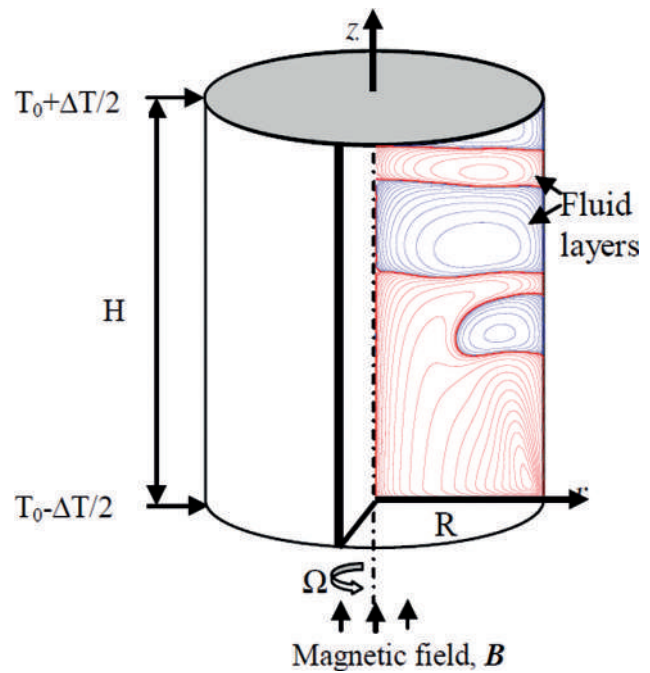


**Figure 1.** Flow geometry and schematic of fluid layers.

aspect ratios ($\gamma$=H/R=2.5, 2.0, and 1.5) are compared, as well as three fluids (Mercury, lead-lithium alloy, and molten lithium). The laminar swirling flow in this situation is characterized by the incompressibility of the three fluids. The temperature difference ($\Delta T$) and a magnetic field are imposed simultaneously in the vertical direction. The swirling motion is generated by the bottom lid, which revolves at a fixed speed of rotation ($\Omega$), while the top wall remains fixed. Because the magnetic Reynolds is so minimal, the magnetic field induction may be ignored and replaced with electromagnetic force (EMF). For three fluids, the following hypotheses are considered: Newtonian; constant; the Boussinesq approximation is valid, the impact of Joule and viscous dissipation are ignored, and at last, radiation is extremely weak.

### Governing Equations

The axisymmetric mathematical equations are expressed in a two-dimensional cylindrical coordinate system, where (($\partial/\partial\theta$=0). As they stand, the governing equations (MHD-mixed convection) are dimensionless as: R (lengths), which). The governing equations (magnetohydrodynamic-mixed convection) are dimensionless as is: $R$ (lengths), the $\Omega R$ (velocities), $\rho(\Omega R)^2$ (pressure), $\Theta = (T - T_0)/\Delta T$ (temperature) and, $B_0\Omega R^2$ (electric potential). So, the dimensionless equations of the steady flow can be described as:

$$\frac{1}{r}\frac{\partial(r.v_r)}{\partial r} + \frac{\partial v_z}{\partial z} = 0 \qquad (1)$$

$$v_r \frac{\partial v_r}{\partial r} + v_z \frac{\partial v_r}{\partial z} - \left( \frac{v_\theta^2}{r} - \frac{\partial p}{\partial r} \right) - \frac{1}{Re}$$
$$\left( \frac{\partial^2 v_r}{dr^2} + \frac{1}{r} \frac{\partial v_r}{\partial r} - \frac{v_r}{r^2} + \frac{\partial^2 v_r}{dz^2} \right) = \frac{Ha^2}{Re} F_{Lr} \quad (2)$$

$$v_r \frac{\partial v_z}{\partial r} + v_z \frac{\partial v_z}{\partial z} + \frac{\partial p}{\partial z} - \frac{1}{Re} \left( \frac{\partial^2 v_z}{dr^2} + \frac{1}{r} \frac{\partial v_z}{\partial r} + \frac{\partial^2 v_r}{dz^2} \right)$$
$$= Ri\Theta + \frac{Ha^2}{Re} F_{Lz} \quad (3)$$

$$v_r \frac{\partial v_\theta}{\partial r} + \frac{v_r v_\theta}{r} + v_z \frac{\partial v_\theta}{\partial z} - \frac{1}{Re}$$
$$\left( \frac{\partial^2 v_\theta}{dr^2} + \frac{1}{r} \frac{\partial v_\theta}{\partial r} - \frac{v_\theta}{r^2} + \frac{\partial^2 v_\theta}{dz^2} \right) \quad (4)$$
$$= \frac{Ha^2}{Re} F_{L\theta}$$

$$v_r \frac{\partial \Theta}{\partial r} + v_z \frac{\partial \Theta}{\partial z} - \frac{1}{Re\,Pr} \left( \frac{\partial^2 \Theta}{dr^2} + \frac{1}{r} \frac{\partial \Theta}{\partial r} + \frac{\partial^2 \Theta}{dz^2} \right) = 0 \quad (5)$$

The interaction of convective flow with the magnetic field induces the electric current:

$$J = \sigma(V \times B + E) \quad (6)$$

The velocity vector $V$ ($v_r$, $v_\theta$, $v_z$), hence the radial, axial, and azimuthal velocity components are denoted ($v_r$, $v_z$ and $v_\theta$), respectively. $E = -\nabla\Phi$ is the electric charges and $\sigma$ is the electric conductivity. The electric potential is given by the divergence of electric current $\nabla J = 0$:

$$\frac{1}{r} \frac{\partial}{\partial r} \left( r \frac{\partial \Phi}{\partial r} \right) + \frac{\partial^2 \Phi}{\partial z^2} - \frac{v_\theta}{r} - \frac{\partial v_\theta}{\partial r} = 0 \quad (7)$$

$$F_{Lorentz} = \vec{J} X \vec{B} \quad (8)$$

The components of EMF( Lorentz force, $F_{Lorentz}$) are:

$$\begin{cases} F_{Lr} = -V_r \\ F_{LZ} = 0 \\ F_{L\theta} = \dfrac{\partial \Phi}{\partial r} - v_\theta, \end{cases} \quad \text{and the dimensionless electric currents are:} \quad \begin{cases} J_r = \dfrac{\partial \Phi}{\partial R} + v_\theta \\ J_Z = \dfrac{\partial \Phi}{\partial z} \\ J_\theta = -v_r, \end{cases} \quad (9)$$

Equation (4) is independent of the $v_r$, $v_z$ components. As a result, the coupled equations (Eqs. (4) and (7)) may be used to simplify the computations. The Hartmann number is modest in our research, thus we may use the following simplification: $(\partial\Phi/\partial r \ll v_\theta)$. As a result, we obtain $F_{L\theta} \approx -v_\theta$ and the electric current $J_r \approx v_\theta$, respectively.

Here denote that, density $(\rho)$, kinematic viscosity $(v)$, thermal expansion $(\beta)$, thermal diffusivity $(\alpha)$, and electric conductivity $(\sigma_e)$. The following parameters $Ha$, $Re$, $Ri$, and $Pr$ are defined as follows:

$Ha = B_0 R\sqrt{\sigma_e/(v\rho)}$ define the rapport between the electromagnetic force and viscous force, where named Hartmann number.

$Re = \Omega R^2/v$ is the Reynolds number, which shows the relationship between inertial and viscous forces.

$Ri = \beta g\Delta T/\Omega^2 R$ is the Richardson number, which represents the potential kinetic energy relationship.

$Pr = v/\alpha$ is the Prandtl number, defined as the momentum diffusivity to thermal diffusivity ratio.

All the boundary conditions are shown in Table 1 shows. The cylinder walls are presumed to have no-slip characteristics ($v_r = v_\theta = v_z = 0$) and electrically insulated.

To implement the GITT approach the stream function formulation is employed [10, 26, 27]. To produce a system of second and fourth-order partial differential equations, we need to follow the following steps. The first step is to remove the pressure field by expressing the streamfunction $\Psi(r,z)$ as:

$$v_r = \frac{1}{r} \frac{\partial \Psi}{\partial r}, v_z = -\frac{1}{r} \frac{\partial \Psi}{\partial r} \quad (10)$$

The second step is to make the differentiation of Eqs. (2) and (3) to z and r, respectively. Step three is to subtract the resulting equations, and use the streamfunction definition.

**Table 1.** The boundary conditions

| Boundary | Radial velocity | Axial velocity | Azimuthal velocity | Temperature |
|---|---|---|---|---|
| $r = 0, 0 \leq z \leq \gamma$ | $v_r = 0$ | $(\partial v_z)/\partial r = 0$ | $v_\theta = 0$ | $\partial\Theta/\partial r = 0$ |
| $r = 1, 0 \leq z \leq \gamma$ | $v_r = 0$ | $v_z = 0$ | $v_\theta = 0$ | $\partial\Theta/\partial r = 0$ |
| $z = 0, 0 \leq r \leq 1$ | $v_r = 0$ | $v_z = 0$ | $v_\theta = 0$ | $\Theta = -0.5$ |
| $z = \gamma, 0 \leq r \leq 1$ | $v_r = 0$ | $v_z = 0$ | $v_\theta = 0$ | $\Theta = 0.5$ |

$$\frac{1}{r}\frac{\partial\Psi}{\partial z}\frac{\partial(\exists^2\Psi)}{\partial r} - \frac{1}{r}\frac{\partial\Psi}{\partial r}\frac{\partial(\exists^2\Psi)}{\partial z} - \frac{2}{r}\frac{\partial\Psi}{\partial z}\exists^2\Psi - 2v_\theta\frac{\partial v_\theta}{\partial z}$$
$$-\frac{1}{Re}\exists^4\Psi = -Rir\frac{\partial\Theta}{\partial r} - \frac{Ha^2}{Re}\frac{\partial^2\Psi}{\partial z^2} \quad (11)$$

$$\frac{1}{r}\frac{\partial\Psi}{\partial z}\left(\frac{\partial v_\theta}{\partial r} + \frac{v_\theta}{r}\right) - \frac{1}{r}\frac{\partial\Psi}{\partial r}\frac{\partial v_\theta}{\partial z} - \frac{1}{Re}$$
$$\left(\frac{\partial^2 v_\theta}{\partial r^2} + \frac{1}{r}\frac{\partial v_\theta}{\partial r} - \frac{v_\theta}{r^2} + \frac{\partial^2 v_\theta}{\partial z^2}\right) = \frac{Ha^2}{Re}(v_\theta) \quad (12)$$

$$\frac{1}{r}\frac{\partial\Psi}{\partial z}\frac{\partial\Theta}{\partial z} - \frac{1}{r}\frac{\partial\Psi}{\partial r}\frac{\partial\Theta}{\partial z} = \frac{1}{Re\,Pr}\nabla^2\Theta \quad (13)$$

$$v_\theta(0,z) = 0; \frac{\partial\Theta(0,z)}{\partial r} = 0, \quad \frac{\partial}{\partial r}\left[\frac{1}{r}\frac{\partial\Psi(r,z)}{\partial r}\right]_{r=0} = 0;$$
$$\left[\frac{\Psi(r,z)}{r}\right]_{r=0} = 0 \quad (14)$$

$$v_\theta(1,z) = 0; \frac{\partial\Theta(1,z)}{\partial r} = 0; \Psi(1,z) = 0; \frac{\partial\Psi(1,z)}{\partial r} = 0 \quad (15)$$

$$v_\theta(r,0) = r; \Theta(r,0) = -\frac{1}{2}; \Psi(r,0) = 0; \frac{\partial\Psi(r,0)}{\partial z} = 0 \quad (16)$$

$$v_\theta(r,\gamma) = 0; \Theta(r,\gamma) = \frac{1}{2}; \Psi(r,\gamma) = 0; \frac{\partial\Psi(r,\gamma)}{\partial z} = 0 \quad (17)$$

- operators $\exists^2$, $\exists^4$ and $\nabla^2$ are defined as:

$$\exists^2 = \frac{\partial^2}{\partial r^2} - \frac{1}{r}\frac{\partial}{\partial r} + \frac{\partial^2}{\partial r^2} \quad (18)$$

$$\exists^4 = \exists^2(\exists^2) = \frac{\partial^4}{\partial r^4} - \frac{2}{r}\frac{\partial^3}{\partial r^3} + \frac{3}{r^3}\frac{\partial^2}{\partial r^2} - \frac{3}{r^3}\frac{\partial}{\partial r}$$
$$-\frac{2}{r}\frac{\partial^3}{\partial r\partial z^3} + 2\frac{\partial^4}{\partial r^2\partial z^2} + \frac{\partial^4}{\partial z^4} \quad (19)$$

$$\nabla^4 = \frac{\partial^2}{\partial r^2} + \frac{1}{r}\frac{\partial}{\partial r} + \frac{\partial^2}{\partial z^2} \quad (20)$$

**Solution methodology**

The GITT approach requires three phases. By choosing an appropriate eigenvalue situation, the initial step is to supply the eigenvalues and, as a result, the eigenfunctions. The second step decrypts the integral transform pair. Finally, Eqs. (11, and13) are transformed by integral. The steps methodology is more detailed in reference [10,27].

**Table 2.** Number of the grid points $N_\psi, N_\theta$, and $N_\Theta$ in the final mesh

| Cases | 0≤Ha≤10 | 11<Ha≤20 | 21<Ha≤40 |
|---|---|---|---|
| | $N_\psi$ | $N_\theta$ | $N_\Theta$ |
| Case A | 100 | 110 | 120 |
| Case B | 150 | 165 | 180 |
| Case C | 200 | 220 | 240 |

Terms $Ha^2\left(\dfrac{\partial^2\overline{\Psi}_i(z)}{\partial z^2}\right)$ and $Ha^2\bar{v}_{\theta,i}(z)$ that appearing in the nonlinear coupled ordinary differential system(ODEs) represents the body forces due to the induced magnetic field (Lorentz force), where $\overline{\Psi}_i(z)$, $\bar{v}_{\theta,i}(z)$ are the transformed potentials of streamfunction and azimuthal velocity, respectively. Then, the stream function and angular velocity can be used to be recalled the components of the radial and axial velocities by using the inverse formula [10]. Eq. (2) may also be used to calculate the pressure field by inserting the relationships for the ($v_r$, $v_\theta$, $v_z$) and then doing an r-direction analytical integration.

## NUMERICAL METHOD AND GRID CONSIDERED

DBVPFD is the double-precision Fortran subroutine of the IMSL library [28], which has been used to numerically solve the coupled system (ODEs). The finite difference method is used to solve ordinary differential equations. At present, the relative error of $10^{-5}$ is accepted. The mesh size (Table 2) is used to satisfy the adaptive error, several meshes will be used because the Hartmann layers influence the solution. $N_\psi$, $N_\theta$, and $N_\Theta$ are respectively the truncation orders which are shown in Table 2 for three combinations, case A: ($\gamma$=1.5; Re=1500); case B: ($\gamma$ =2.; Re=1855,); and case C: ($\gamma$ =2.5; Re=2400)

## RESULTS AND DISCUSSION

The numerical code's validity is verified by comparing the obtained findings to the numerical and experimental investigation reported by Kharicha et al. [20]. They studied flow in a cylindrical container, which is filled with a viscous fluid (mercury). The steady laminar flow is subject to the presence of a constant magnetic field. Figure 2 depicts the reconstruction of the hydrodynamic ($\Psi$) and electric ($\Psi'$) for the aspect ratio $\gamma$ = 2 and the magnitude Ha. However, the obtained plots of streamlines in Fig. 2a are coherent with the observations of Kharicha et al. [20]. The electric current streamlines are traced using the electric streamfunction $\psi'$ (Fig.2b) defined as: $J_r = 1/r.\partial\Psi'/\partial z$ [29]. Finally, it should be noted that our results are presented to the left of each figure.
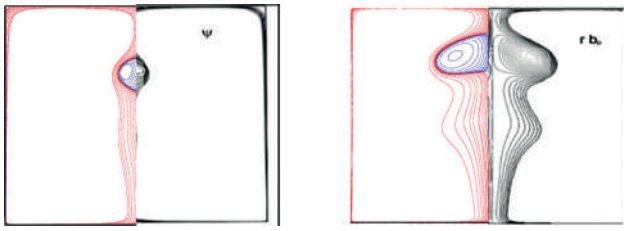
**Figure 2.** Validation with numerical and experimental investigation of Kharicha et al. [20]. Our results are presented to the left of each figure, which represents the hydrodynamic streamfunction ($\Psi$) and electric one ($\Psi'$)

## Buoyancy influence on the fluid layers and vortex breakdown

Three Prandtl values, Pr = 0.025, 0.032, and 0.065, as well as three aspect ratios and Reynolds numbers, were computed. The studied Richardson number falls between 0 and 2.0. The respective combinations are case A: ($\gamma$ = 1.5; Re = 1500); case B: ($\gamma$ = 2.; Re = 1855,); and case C: ($\gamma$ = 2.5; Re = 2400). The definition of the number of layers is the distinct recirculating fluid formed in the meridional plane.

### Case of Pr=0.025

To examine how buoyancy affects the creation of fluid layers as well as the behavior of vortex breakdown (position and suppression), taking the case of Mercury (saturated liquid at 293°K), corresponding to Pr=0.025. The basic flow case (Ri = 0) corresponds to forced convection which results in the decoupling between the velocity and temperature fields. In case (A) corresponding to Re =1500 and H/R=1.5, one axisymmetric bubble is formed near the mid-axis of the cylinder when Ri =0 as shown in Fig. 3. In this situation, the revolving disk exerts a centrifugal force on the fluid, accelerating it radially to the sidewall and in spiraling it up. When the fluid is stopped by the side wall, it will turn upwards, consequently, jets will be produced. The upward jets and downward flow result in the creation of a concentrated vortex. According to Vogel [1], this vortex undergoes breakdown and appears on the cylinder axis. Fig. 3a indicates that the breakdown location is at z = 0.969 and on the r-axis is at |r| = 0.145 for case (A). However, buoyancy forces impact the pressure gradient, which tends to reduce non-homogeneities, thus the vortex breakdown can be predicted to disappear when Ri=0.1. In this case, the fluid moves quasi-rigid with an intermediate velocity between the end disks. However, the flow is under the azimuthal equilibrium generated by the viscous stress. When Ri = 1 (Fig. 3-c), the buoyancy acting on the fluid nearby of a hot disk is much stronger than the force of inertia. Two cells dominate secondary flow and fluid cannot strain downward. Above z >1, a corner recirculating (counter-rotating flow) occurred near the top stationary disk, which

has a smaller size (plot in A of Fig. 3c). As the Richardson number is increased to Ri=2, this region expands and occupies the upper part of the cylinder (Fig. 3e). Fluid recirculation is greatest when Ri=0 ($\psi_{max}$ =0.0083), and when Ri>0, the $\psi_{max}$ decrease quickly with the Ri and are 0.0079, 0.0071, 0.0069, and 0.0067 at Ri =0.1, 1.0, 1.5 and 2, respectively.

Plots in Fig. 3's second row develop scenario B for Ri=0, which shows a two-bubble vortex breakdown. The small and the big bubble are superimposed and centered on the z-axis at 0.92 and 1.41, respectively. However, in this case, two upward jets are apparent near the walls. A short increase in the Richardson number to Ri =0.1 (Fig. 3b) causes the disappearance of vortex breakdown bubbles. To examine the transition from a single-layer to a double-layer flow structure, the range of Ri=0.5 to 2 was performed and summarized in the second line of Fig. 3. Due to the counter-rotating flow, two lobes centered at |r| =0.74 and z=1.30 become visible at Ri=1. This is seen in Fig. 3 (c) in scenario B (Ri=1), where the isoline reveals the formation of a double-layer flow pattern. If Ri continues to rise (from 1.5 to 2),counter-rotating cells develop near the upper disc in the form of a double lobe.

Case C is given in the third row of Fig.3, where the effect of Richardson's number is shown. According to Omi and Iwatsu [8], a bubble with the shape of a "cucumber" is formed when two bubbles join. The fluid rotates quasi-rigidly ($\Psi_{min}$=0) when Ri=0.1 because vortex breakdown is suppressed in this case (Fig 3b). When Ri is set to 1, three fluid layers arise. In the upper and lower cylinders, there is one clockwise recirculation zone and two counterclockwise recirculation sections, respectively. In the range of $1.5 \leq$ Re $\leq 2$, up to three layers manifest at Ri = 1.5 and five layers stratify when Ri = 2 (Figs. 3d–3e).

Figure 4 depicts the evolution of fluid layer creation versus the Richardson number, where the fluid is a lead-lithium alloy with the Prandtl number Pr=0.025. When Ri=0, the flow is characterized by a single layer with a concentrated vortex breakdown. In the range Ri≤0.6, the flow is defined by a single layer; however, beyond Ri >0.6, a second layer is visible. It was also discovered that as the Richardson number grows, so does the number of layers in situation A. When Ri $\geq$ 0.4, a second layer is visible in the case of B. Case C, shows an increase in the number of layers formed: three layers when Ri is 1, four layers between 1.9 and Ri 1.7, and five layers when Ri surpasses 1.9.

### Case of Pr=0.032

The situation where the fluid is (PbLi 17), which corresponds to Pr=0.032 is shown in Fig 5. the flow structure in the scenario when Pr=0.032 is almost identical when Pr=0.025, in case (A) because the buoyancy effect is negligible. Exactly like in the example given for Pr=0.025, increasing the value of Ri leads the vortex breakdown bubbles to cease to be visible at Ri= 0.1, as in case A. (Fig. 5b). When Ri = 1.0, a tiny recirculation zone develops under the top
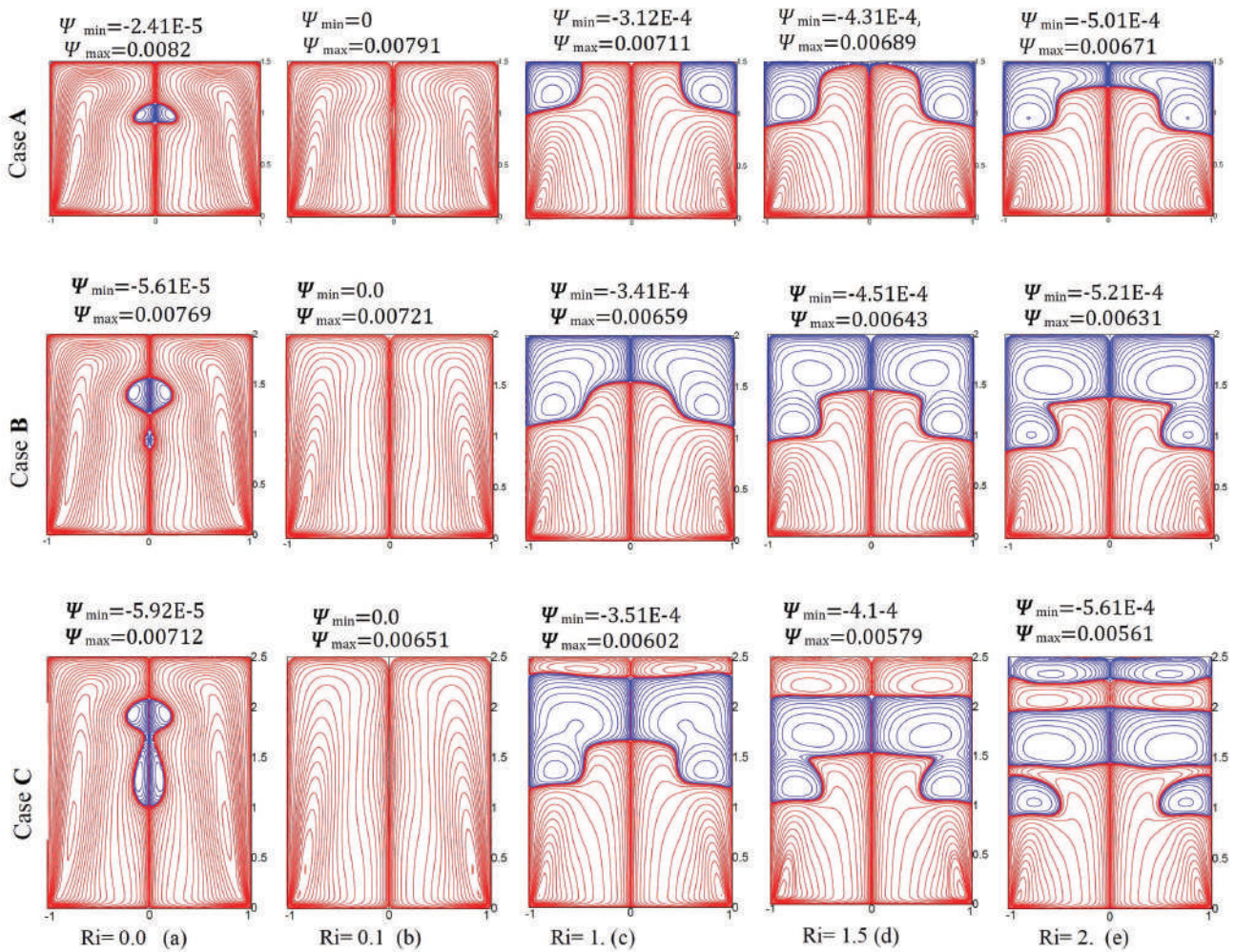
**Figure 3.** Flow pattern when Pr=0.025 with increasing Richardson numbers.
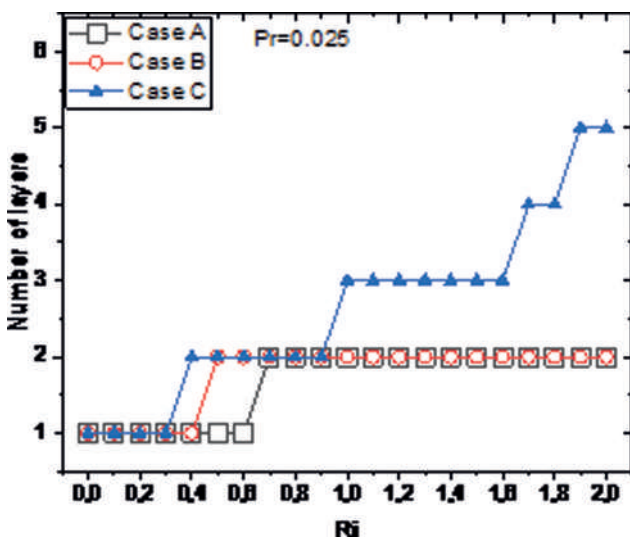


**Figure 4.** Progression of the number of layers VS Ri in case of Pr = 0.025.

stationary disk (Fig. 5c). However, in this scenario, fluid recirculation is greatest when Ri=0 ($\Psi_{max}$ =0.0083) and rapidly drops with increasing Richardson number to $\Psi$max =0.0066 when Ri=2. The scenario of Ri=0.1 in the second row of Fig. 5 is virtually identical to what was found in the previous section; furthermore, when Ri = 0.1, all two bubbles have vanished (Fig. 5c). The transition from a single layer to a double layer flow structure is observed near to Ri =1.0, where the $\Psi_{max}$ at this state is 0.0065. When Ri is raised above 1.5, more transitions occur, resulting in a three-layered structure. A tiny clockwise flow area has located close to the fixed top disk, with a reduction in jets ($\Psi_{max}$=0.0063), as shown in Fig.4b. When Ri =2 this new clockwise region of flow has grown and led to a four-layer flow structure (Fig. 5e). As a result, increasing the Richardson number leads to a decrease in $\Psi_{max}$.

The buoyancy effect on the migration to a multi-layered is the strongest in instance C. Fig.5(C) shows the results when the Richardson number goes from 0 to 2. When Ri = 0 the
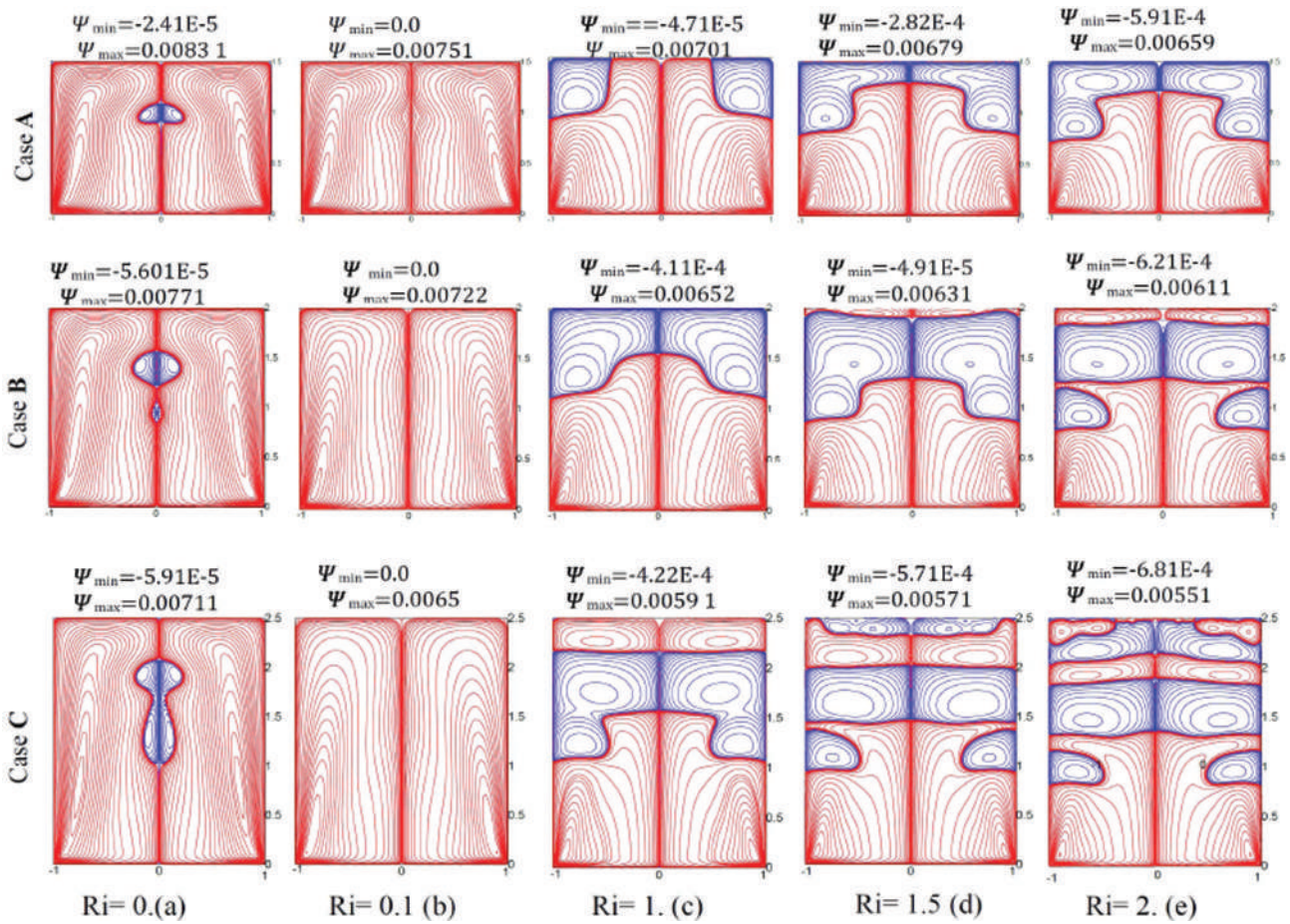
**Figure 5.** Flow pattern when Pr=0.032 with increasing Richardson numbers.

stream function attains the maximum value ($\Psi_{max}$=0.0071) and decreases as Ri is increased toward $\Psi_{max}$ =0.0055 at Ri = 2.0, as shown in Fig. 5(C). The two 'egg' bubbles centered along the cylinder axis(Ri =0.0) disappear at Ri=0.1. If the temperature gradient is reasonable, the Ekmàn suction in the core of the cylinder decreases, allowing multi-layers to be formed (Fig. 5c). When Ri = 1.5, five layers are developed, and at Ri = 2.0, six layers are formed, however, some layers do not cover the complete area of the cylinder.

Figure 6 shows the progression of fluid layer formation vs the Richardson number, with the Prandtl number set at 0.032. The flow has a single layer for Ri ≤0.4, but the rises in Richardson number beyond 0.5 give birth to a second stratified layer. The effect of raising Richardson's number on layer creation is larger in the case of (B) than in case A. When Ri=2, a four-layer flow structure is found in this situation (case B). In scenario (C), up to five stacked recirculating zones are discovered in the case of Ri = 1.5, while six layers are recorded in the Ri = 2 situation.
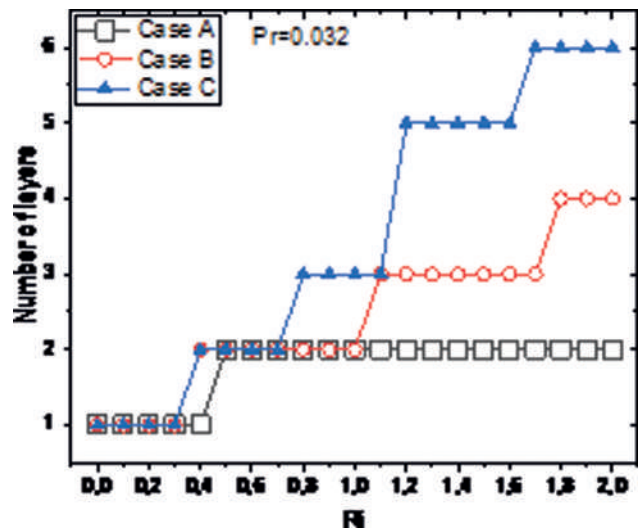


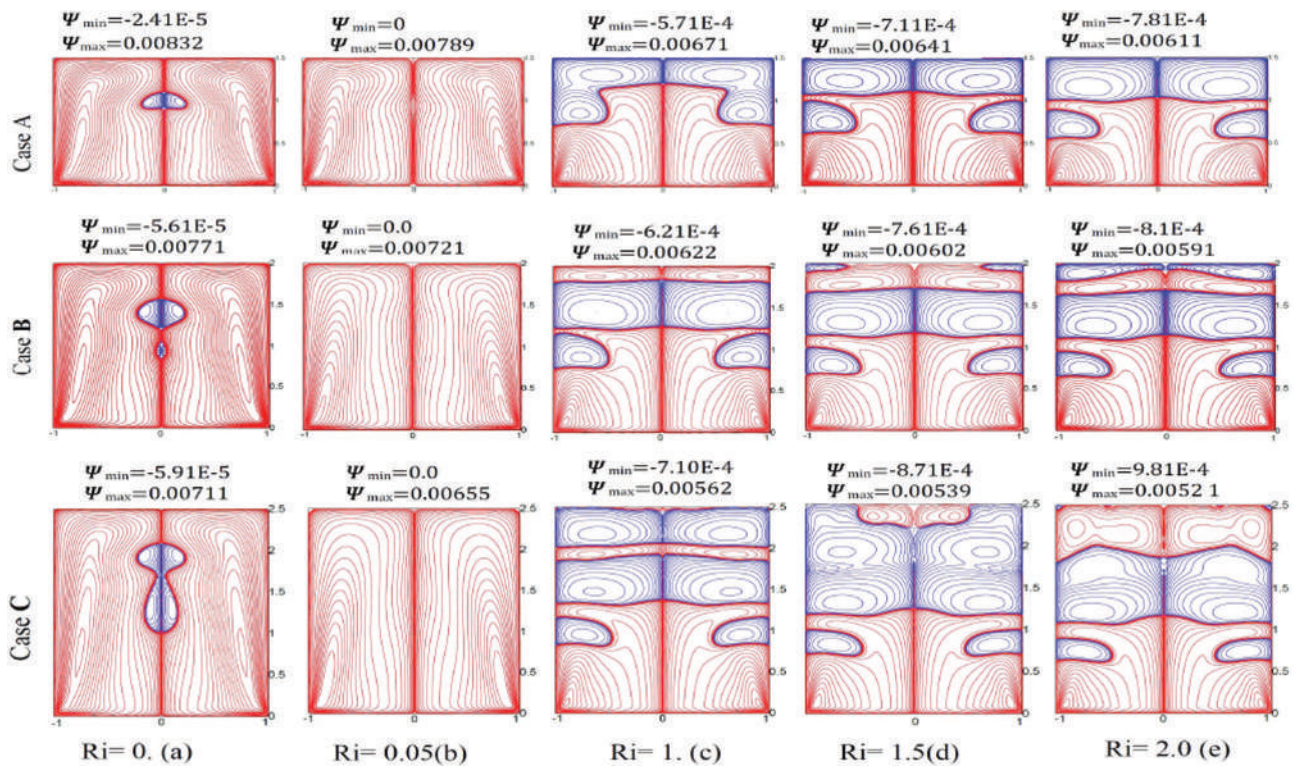**Figure 6.** Growth of the number of layers VS Ri in the case for Pr=0.032.

**Figure 7.** Flow pattern when Pr=0.064 with increasing Richardson numbers.

***Case of Pr=0.064***

The buoyancy action in examples A, B, and C is shown in Fig.7, in this case, the fluid corresponds to molten lithium at 454°K with Pr=0.064. Here (case A), the breakdown disappears when Ri increases to 0.05. The isolines in scenario (A) for Ri=0.05 and 2 demonstrate a drop in the maximum stream function, which is 0.0079 and 0.0061, respectively (Fig. 7). When Ri = 1 of case (A), a double-lobe structure with counter-current emerges and occupies the whole top portion of the cylinder, as seen by the streamlines (Fig. 7c). In example (A), increasing Ri to 1.5 and 2, respectively, induces a disintegration in the countercurrent area, resulting in three-layered recirculation zones (Fig. 7d-e).

Multiple fluid layers when Ri in case B goes from 1 to 2 with an increment of 0.5 are shown in Fig. 7. A more increase in Ri leads to the formation of new fluid layers, and up to four layered recirculating zones appear for Ri = 1 and five such zones are noted for Ri = 1.5 and 2, respectively. It should be noted that the layers formed do not spread throughout the full meridian, but rather concentrate in the middle zone between z =0.73 and |r| = 0.91.

Case C demonstrates that the temperature gradient impact is larger when compared to the two preceding cases (A and B), as seen in Fig. 7. Here also the results show that when Ri=0.05, the vortex breakdown is suppressed. The $\psi_{max}$ decreases with increasing Ri and are 0.0065 and 0.0052 at Ri=0.05 and Ri=2, respectively. When Ri=1, six layers are

formed (plots in (C) of Fig. 7c), and these layers continue to merge, as when Ri>1. By Ri =1.5 the counterclockwise recirculation region disappears between two clockwise recirculation regions, then merged into a single one to occupy the most of upper half-cylinder, which has a four-lobe structure. The decrease in the number of layering can be observed in the range of 1≤Ri ≤2.

Diagrams similar to the one presented in cases Pr=0.025 and Pr=0.032 are then constructed to present the case of Pr= 0.065, in which the change in the total fluid layers is given in Fig. 8a. It is observed in this figure that the effect of vertical temperature difference on the flow pattern is to lead the meridional flow into layered structures. The behavior in cases A and B is the same as in the state of Pr = 0.032. It is obvious that in example A, the flow has a single layer, which occurs at Ri ≤0.05. Around Ri 0.05, the flow was dominated by a single layer; however, at Ri=0.5 and 1.5, the creation of a second layer and three layers was seen. When Ri=2, a five-layer structure is found in the case of B. This behavior is in contrast to the previous cases of A and B in which a drop in the number of layering can be observed for case C when Ri>1.2.

Figure 8b depicts the development of the number of layers versus Richardson number in Case (C), in which three Prandtl values are examined. According to Fig. 8b, the fluid qualities represented by the Prandtl number, *Pr* have a considerable influence on the overall number of fluid layers
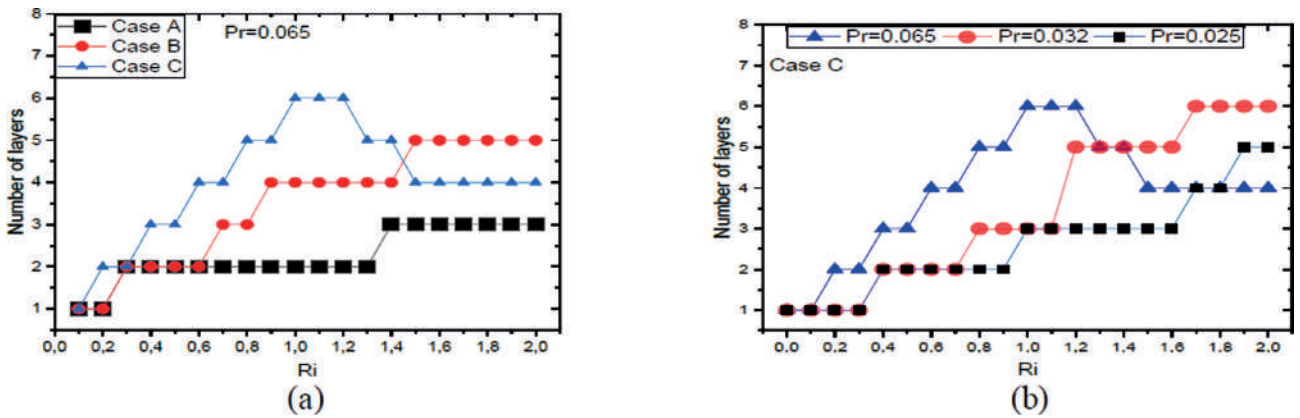
**Figure 8.** Evolution of the number of layers versus Richardson number: (a) Pr=0.065 and (b) for all Prandtl numbers.
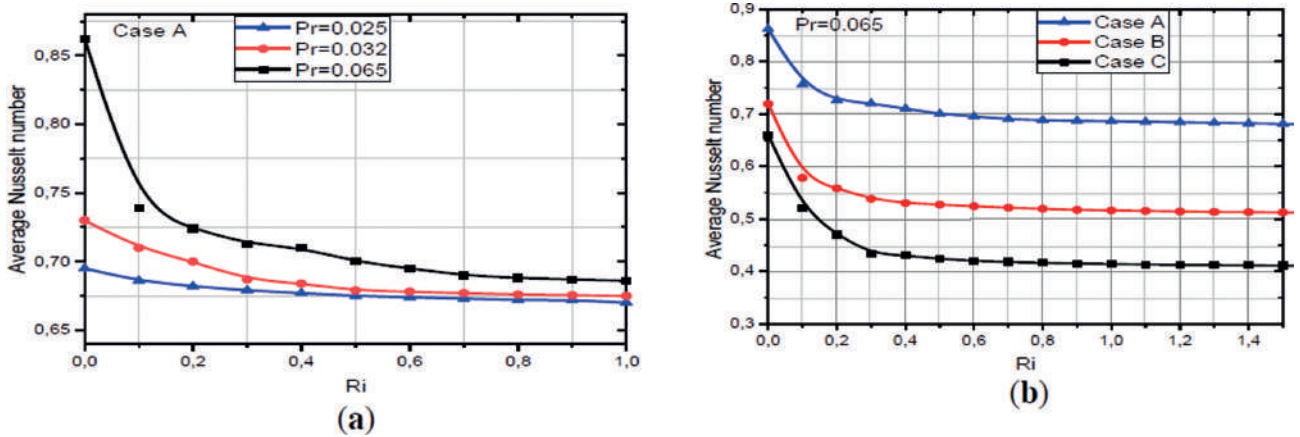


**Figure 9.** Effect of the Richardson number on the average Nusselt number.

formed. As a result, the number of fluid layers grows as Ri increases in both the Pr=0.025 and Pr=0.032 situations, as seen in Fig. 8b. On the contrary, when Pr=0.065, the number of fluid sheets increases, but this increase is not monotone since when it surpasses Ri > 1.2, the number of fluid sheets decreases.

**Heat transfer**

The Nusselt number and a variety of factors are used to examine heat transfer throughout the section that follows. The question here is whether the existence or absence of fluid stratification is governed by the coupling of the Reynolds number and the aspect ratio. Figure 9a depicts the development of the average Nusselt number with Ri for various *Pr* in Case A. It is demonstrated here that the average Nusselt number decreases with increasing Ri for all Prandtl numbers. It is well known that increasing *Pr* improves advective transport. This is expressed by the average Nusselt number, in which at a constant value of Ri, a rising Nusselt number is seen if *Pr* also rises. (Fig. 9a).

In the instance of Pr=0.065, the average Nusselt number vs Ri is plotted, as shown in Fig. 9b, which compares three combinations (A, B, and C). The figures in Fig.9a demonstrate that as Ri grows, the drops become monotone and correspond to the inverse of the aspect ratio. Take note that 1/H=0.4 for H/R=2.5, 0.5 for H/R=2.0, and 0.66 for H/R=1.5, which are the conduction limit values. Ri=0.86 yields the highest average Nusselt number value in case (A), in which the meridian flow is characterized by a single layer. Similarly, the average Nusselt number in cases B and C takes extreme values when Ri= 0 and 0.75 and 0.70, respectively. Only at the upper heated disk do the effects of natural convection remain. The lighter hot fluid rests on the heavier cold fluid, which leads to a physical phenomenon translated by the thermal isolation between the upper hot disk and the lower cold disk. This isolation becomes more important when the number of fluid layers is large.

**Magnetic effect on fluid layers**

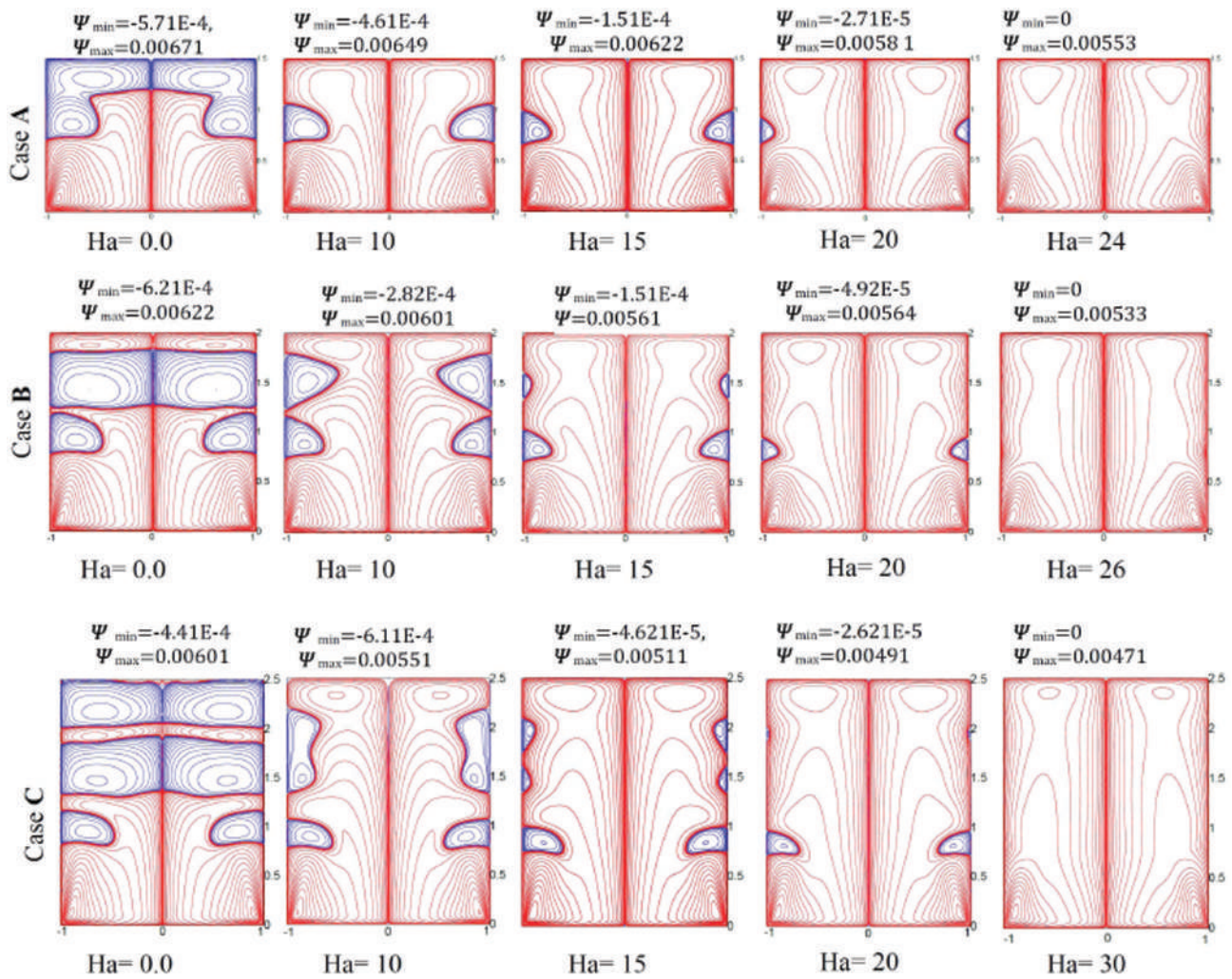To explore the impacts of electromagnétic force on layering position or suppression, consider the situations

**Figure 10.** Stream function plots for Ri=1 when Pr = 0.065.

of Ri=1.0 for the largest Prandtl number, $Pr==0.065$, and in the three cases (i.e. A, B, and C, respectively). The case without magnetic field of Ri = 1 schematized by hydrodynamic streamlines (Fig 10) shows the existence of an upper layer characterized by a double lobe. The electromagnetic force induces various interesting changes in the fluid layers, as seen by the streamlines (Fig. 10). The most important point is that when the magnetic field magnitude (Ha) increases, the counter-flow layers migrate farther from the side walls. Another observation that may be made here is that at a critical value of Ha, the counter-flow cells will vanish altogether. When Ha = 10, the cells at the top of the clockwise recirculation diminish in size and move toward the side wall. The counterclockwise recirculation zone, on the other hand, expands until it occupies the whole top half of the cylinder. The r-central location of the tiny toroidal zone increases as Ha increases, whereas the z-central position decreases significantly. When $Ha_{cr}=24$, the tiny toroidal vortex seen at Ha=20 decreases and finally vanishes.

When Ri=1, the flow is represented by a single layer with a maximum of $\Psi$ is 0.0055.

At Ha=10, only two layers are visible in the case of B, whereas four layers are visible in the case of B without a magnetic field (Ha=0). In this scenario, we have two small clockwise vortices that connect to the side wall. The top vortex for Ha=15 shrinks and disappears at Ha=20, whereas the below vortex resists up to Ha=26. At Ha=20, a small toroidal vortex with a maximum stream function of 0.0056 appears and then vanishes. At Hacr=26, the flow is dominated by a single layer with a maximum of 0.0053.

Case C seen at Pr = 0.065 in Fig. 10 shows at Ri = 1.0, the effect of raising Ha. When Ha=10, the number of layers decreases to three, whereas six layers were previously discovered without a magnetic field (Ha=0). The flow in the upper section separates into two vortices at Ha=15, in which the z-central of these vortices increases as Ha increases, but the r-central location decreases. The size of this vortex shrinks as Ha increases and gives a two-cell flow
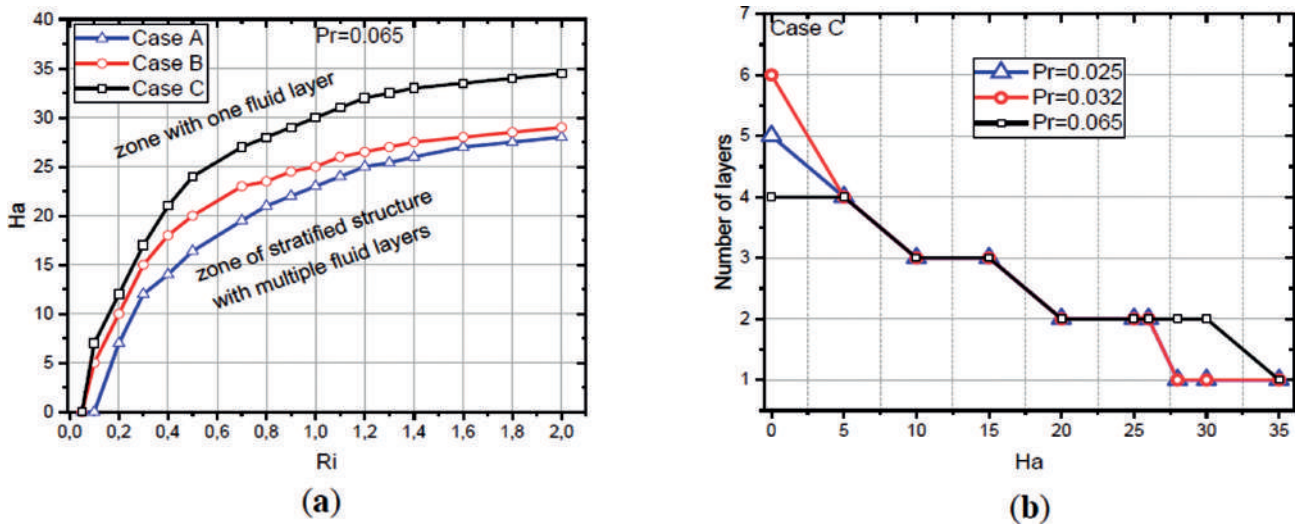
**Figure 11. (a)** Stability diagram of the transition from multiple fluid layers to a single layer **(b)** Number of layers vs *Ha*.

pattern at Ha = 20. The third line in Fig.10e illustrates a small toroidal vortex positioned downwards that still resists and dissipates at Ha = 25 and evaporates at Ha = 30.

Figure 11a depicts the development of the critical Hartmann number with Richardson number, as seen in the ($H_{cr}$-Ri) plot for Pr=0.065. Figure 11a shows three alternative curves that limit the domains with and without stratified fluid layers. These three cases show a monotonic increase between Ri land $Ha_{cr}$. Furthermore, rising Ha until critical value suppresses the fluid layers at a constant value of Ri, i.e. layering ceases once the amplitude of Ha exceeds a crucial point. For a constant Richardson number, the magnitudes of Ha in cases A and B are less than those found in case C. For example, when Ri = 1.0, the critical Hartmann number magnitudes for situations A, B, and C are Ha=23, 25, and 30, respectively.

The diagram (Ha-Number of layers) that compares the three fluids (Pr = 0.025, 0.032, and 0.065, respectively) represents the magnetic field-reducing influence on the number of fluid layers created by the buoyancy effect. For Ha=0 and when Pr equals 0.032, six layers were generated, and five and four layers are developed for Pr=0.025,and Pr=0065, respectively. From Ha=5, the number of layers for these three fluids tends to decrease until there is just one layer for a suitable intensity of Ha. When $Ha_{cr}$ is equal to 26, 28, or 35. For Pr=0.025, 0.032, and 0.065, the flow is described by a single flow cell. As a result, the resultant layer structures are impacted by the Prandtl Number, which impacts either growth or decrease.

## CONCLUSION

The laminar vortex decomposition and the size of the fluid layer formed in cylindrical containers due to combined magnetic field and buoyancy forces have been studied numerically. To solve the governing equations, the GITT method was utilized. Three combinations (Re, H/R) were compared and developed for three different viscous fluids. The main results obtained are as follows:

- In both cases, A and B, increasing Richardson number to 0.1 leads to a single layer that occupied the fluid domain but for case C the value of Ri=0.05 is sufficient to eliminate vortex breakdown.
- Increases in the values of the Richardson number have a favorable influence on the number of fluid layers.
- In both situations A and B, the number of stratification layers increases as Ri increases, however in case C, the number of fluid layers decreases as the Richardson number amplitude exceeds a critical threshold.
- Because of the isolation phenomena caused by the hot region's fluid layers, the Nusselt number decreases as Ri increases.
- The different curves show that the increase in the magnetic field diminishes the number of fluid layers.
- Finally, an axial magnetic field may be used to govern the boundaries between structures with many fluid layers and those with a single layer.

## REFERENCES

[1] Vogel HU. Experimentelle Ergebnisse ueber die laminare Stroemung in einem zylindrischen Gehaeuse mit darin rotierender Sceibe. Max-Plank-Institute für Strömungsforschung, Göttingen, Bericht;1968. [Deutsch]

[2] Escudier MP. Observations of the flow produced in a cylindrical container by a rotating endwall. Exp Fluids 1984;2:189–196. [CrossRef]

[3]   Herrada MA, Shtern V. Control of vortex breakdown by temperature gradients. Phys Fluids 2003;15:3468–3477. [CrossRef]

[4]   Dash SC, Singh N. Effects of partial heating of top rotating lid with axial temperature gradient on vortex breakdown in case of axisymmetric stratified lid driven swirling flow. J Therm Eng 2016;2:882–896. [CrossRef]

[5]   Ismadi MZP, Meunier P, Fouras A, Hourigan K. Experimental control of vortex breakdown by density effects. Phys Fluids 2011;23:034104. [CrossRef]

[6]   Ben Hadid H, Henry D, Touihri R. Unsteady three-dimensional buoyancy-driven convection in a circular cylindrical cavity and its damping by magnetic field. J Cryst Growth 1997;180:433–441. [CrossRef]

[7]   Mahfoud B, Bessaïh R. Oscillatory swirling flows in a cylindrical enclosure with co-/counter-rotating end disks submitted to a vertical temperature gradient. Fluid Dyn Mater Process 2012;8:1–26.

[8]   Omi Y, Iwatsu R. Numerical study of swirling flows in cylindrical container with co-/counter-rotating end disks under stable temperature difference. Int J Heat Mass Transf 2005;48:4854–4866. [CrossRef]

[9]   Turan O, Yigit S, Chakraborty N. Effects of wall heating on laminar mixed convection in a cylindrical enclosure with a rotating end wall. Int J Therm Sci 2018;131:80–93. [CrossRef]

[10]  Quaresma N, da Cruz CCS, Cagney N, Cotta RM, Balabani S. Effect of mixed convection on laminar vortex breakdown in a cylindrical enclosure with a rotating bottom plate. Int J Therm Sci 2020;155:106399. [CrossRef]

[11]  Oreper G, Szekely J. The effect of a magnetic field on transport phenomena in a Bridgman-Stockbarger crystal growth. J Cryst Growth 1984;67:405–419. [CrossRef]

[12]  Davidson PA. An Introduction to Magnetohydrodynamics. 1st ed. Cambridge: Cambridge University Press; 2001.

[13]  Mahfoud B, Laouari A, Hadjadj A, Benhacine H. Counter-rotating flow in coaxial cylinders under an axial magnetic field. Eur J Mech B Fluids 2019;78:139–146. [CrossRef]

[14]  Mahfoud B, Benhacine H, Laouari A, Bendjaghlouli A. Magnetohydrodynamic effect on flow structures between coaxial cylinders heated from below. J Thermophys Heat Transf 2020;34:265–274. [CrossRef]

[15]  Mahfoud B, Bessaïh R. Stability of swirling flows with heat transfer in a cylindrical enclosure with co/counter-rotating end disks under an axial magnetic field. Numer Heat Transf A Appl 2012;61:463–482. [CrossRef]

[16]  Mahfoud B, Bessaïh R. Magnetohydrodynamic counter-rotating flow in a cylindrical cavity. Int J Heat Mass Transf 2016;93:175–185. [CrossRef]

[17]  Mahfoud B, Bendjagloli A, Bessaïh R. Magnetohydrodynamic co-rotating flow in a vertical cylindrical container. Numer Heat Transf A Appl 2016;69:1051–1063. [CrossRef]

[18]  Bendjaghlouli A, Mahfoud B, Ameziani DE. Magnetohydrodynamic flow in a truncated conical enclosure. J Therm Eng 2019;5:77–83. [CrossRef]

[19]  Bendjaghlouli A, Ameziani DE, Mahfoud B, Bouragbi L. Magnetohydrodynamic counter rotating flow and heat transfer in a truncated conical container. J Thermophys Heat Transf 2019;33:865–874. [CrossRef]

[20]  Kharicha A, Alemany A, Bornas D. Influence of the magnetic field and the conductance ratio on the mass transfer rotating lid driven flow. Int J Heat Mass Transf 2004;47:1997–2014. [CrossRef]

[21]  Yu Y, Li BW, Thess A. The effect of a uniform magnetic field on vortex breakdown in a cylinder with rotating upper lid. Comput Fluids 2013;88:510–523. [CrossRef]

[22]  Mahfoud B, Bendjaghlouli A. Natural convection of a nanofluid in a conical container. J Therm Eng 2018;4:1713–1723. [CrossRef]

[23]  Laouari A, Mahfoud B, Bessaïh R, Hadjadj A. Hydrodynamic instabilities in swirling flow under axial magnetic field Eur J Mech B Fluids 2021;85:245–260. [CrossRef]

[24]  Colaço J, Dulikravich GS, Orlande HRB. Magnetohydrodynamic simulations using radial basis functions. Int J Heat Mass Transf 2009;52:5932–5939. [CrossRef]

[25]  Cotta RM, Mikhailov MD. Integral transform method. Appl Math Model 1993;17:156–161. [CrossRef]

[26]  Lima JA, Rêgo MGO. On the integral transform solution of low-magnetic MHD flow and heat transfer in the entrance region of a channel. Int J Non-Linear Mech 2013;50:25–39. [CrossRef]

[27]  Matt CFT, Quaresma JNN, Cotta RM. Analysis of magnetohydrodynamic natural convection in closed cavities through integral transforms. Int J Heat Mass Transf 2017; 113:502–513. [CrossRef]

[28]  Rogue Wave Software. IMSL® Fortran Numerical Library, Version 2018, Rogue Wave Software Inc., Boulder, USA, 2018.

[29]  Bojarevičs V, Freibergs JA, Shilov EI, Shcherbinin EV. Electrically Induced Vortical Flows. 1st ed. Netherlands: Kluwer Academic Publishers; 1989. [CrossRef]